Imperfect $O(2)$ symmetry in counter-rotating split-cylinder flow

P. Gutierrez–Castillo[1] and J. M. Lopez[2]
[1)] *Escuela de Ingenierías Industriales, Universidad de Málaga, Campus de Teatinos 29071 Málaga, Spain*
[2)] *School of Mathematical and Statistical Sciences, Arizona State University, Tempe AZ 85287, USA*

(Dated: 1 December 2021)

The effect of a small imperfection in the counter-rotating split-cylinder flow is studied numerically. The defect is characterized by a small parameter ϵ, corresponding to the difference in the magnitude of the rotations in each half of the cylinder. With the two half cylinders not rotating exactly in counter rotation, the $O(2)$ symmetry of the exact counter-rotating case (invariance to azimuthal rotations as well as to an involution consisting of a reflection about the mid-plane composed with a reflection about any meridional plane) is weakly broken. This small defect results in relevant variations in the flow. For slow rotations (characterized by a small Reynolds number), the system remains axisymmetric, with the imperfection only breaking the reflection symmetry about the cylinder half-height. At larger Reynolds numbers, in the absence of the imperfection, axisymmetry is broken resulting in steady states with azimuthal wavenumber m. When axisymmetry is broken in the presence of the imperfection, a background rotation is introduced. Depending on the case and the level of imperfection, either rotating waves or slow-fast dynamics with a mean background rotation are found instead. The interaction between azimuthal wavenumbers $m = 2$ and 3 plays a crucial role in the flow. The flow is analyzed in detail, varying ϵ from a very small value of 0.01%, typical of a natural imperfection in an experimental set-up, to higher values corresponding to forced symmetry breaking. The ramifications of the imperfection on the various solution states found in the exact counter-rotating case for a fixed aspect ratio are investigated.

I. INTRODUCTION

The counter-rotating split cylinder has attracted much recent attention for its potential to develop finite-time blow up in the inviscid limit (Re $\to \infty$, where the Reynolds number Re is the ratio of the viscous to inertial time scales), when the system is constrained to being axisymmetric and axial-reflection symmetric.[1–5] Our interests here are in the nonlinear dynamics at finite Re; the symmetries are broken at Re $\sim 10^2$ — far from the inviscid limit. In Gutierrez-Castillo and Lopez[6], we studied the nonlinear dynamics when the cylinder halves were in exact counter rotation, so that the system is invariant to rotations about the axis, reflections through meridional planes and a reflection about the cylinder mid-height, all combining to give an $O(2)$ symmetry. This is the same symmetry as in the well-studied von Kármán flow, consisting of a stationary cylinder and two exactly counter-rotating endwalls.[7] Here we focus on the effects of imposing small imperfections in the axial reflection symmetry due to small differences in the magnitudes of the rotations of the cylinder halves.

Studies of $O(2)$ symmetry breaking has a long history. Crawford and Knobloch[8,9] and Knobloch[10] presented equivariant singularity theory and normal form analyses of degenerate Hopf bifurcations in $O(2)$-symmetric systems and analyzed the effects of symmetry-breaking perturbations on the unfoldings of these degeneracies. We focus on the simplest degeneracies among the nonlinear terms and assume that the perturbation breaks the Z_2 reflection symmetry leaving a residual $SO(2)$ axisymmetry intact. Chossat[11] also looked at forced symmetry breaking, $O(2) \to SO(2)$, from a theoretical perspective; he focused on what happens to the heteroclinic cycles which are a peculiar aspect of the normal form dynamics.

These types of systems with imperfect $O(2)$ symmetry are not only of theoretical interest but also of importance from a practical engineering perspective. Focusing on the experimental recreation of the counter-rotating split cylinder, it is usual that each half of the cylinder is driven by a different motor leading to a small asymmetry in the system. The difference in the rotation rates typically being of the order of 0.01% in a well-designed experiment.[12] But even such small imperfections can lead to results far different from those in a perfect system. The effects of small imperfections in Taylor–Couette flow have been studied numerically and theoretically,[13,14] motivated by peculiar experimental observations,[15] which were suggested to be a consequence of small imperfections. In those studies, the imperfect $SO(2)$ symmetry was studied, which is much simpler than the imperfect $O(2)$ symmetry analyzed in this paper, but it still results in very complex dynamics. Symmetry imperfections in any experiment, even when they are small, should be taken into account and their influence understood. This could be further used to control the influence of the asymmetry. Recently, it was found that features typical of spontaneous symmetry breaking, while destroyed by one asymmetry, can be restored by introducing a second asymmetry.[16] Their results were restricted to the Z_2 symmetry group but they provide a starting point for analyzing other symmetry groups.

It can be important to distinguish between spontaneous symmetry breaking in a perfectly symmetric sys-

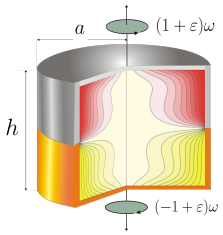

FIG. 1. Schematic of the flow system; the inset shows contours of the azimuthal velocity, v, for the basic state BS at $\mathrm{Re}=120$, $\Gamma=1.45$ and $\epsilon=0.03$.

tem and forced symmetry breaking due to imperfections in the system. Both can lead to complex nonlinear dynamics, but these can be very different in the two systems. Of course, in a physical experiment, both spontaneous and forced symmetry breaking will typically be present, and disentangling the two can be a challenge. The von Kármán flow with endwall blades driven at large Re is a typical example where this occurs.[17–19] In particular, Nore, Moisy, and Quartier[20] experimentally studied the effects of imperfection and the noise on the near-heteroclinic cycles found in the von Kármán flow near the 1:2 interaction (a codimension-2 point in parameter space where the $SO(2)$ symmetry is broken to states with either azimuthal wavenumbers $m=1$ or $m=2$). Theoretical consideration of the dynamics near the 1:2 spatial resonance in systems with broken $O(2)$ symmetry were described in Porter and Knobloch[21]. They assumed their system to remain $SO(2)$ symmetric and focused their attention on the behavior that replaces the structurally stable heteroclinic cycles present in the $O(2)$-symmetric system. The symmetry-breaking destroys these cycles, and introduces a variety of new bifurcations into the system, some of which are associated with complex behavior. Their results are from normal form analysis, and they "propose to compare our results with three-dimensional simulations of the von Kármán vortex flow between nearly counter-rotating disks in a future publication," but this remains to be done.

In this paper, we present a study of the effects of small forced symmetry breaking due to imperfect counter rotation, and compare the solutions with the exactly counter-rotating case.

II. GOVERNING EQUATIONS AND NUMERICAL METHODS

The flow of a fluid of kinematic viscosity ν contained in a differentially rotating split cylinder is studied numerically. The cylinder of radius a and length h is split at mid-height and the two halves are counter rotating with angular speeds $(\epsilon\pm1)\omega$, with $0\le\epsilon\ll1$. Figure 1 shows a schematic of the system. Using a as the length scale and a^2/ν as the time scale, the non-dimensional Navier–Stokes equations are

$$\partial_t\boldsymbol{u}+(\boldsymbol{u}\cdot\nabla)\boldsymbol{u}=-\nabla p+\nabla^2\boldsymbol{u},\quad \nabla\cdot\boldsymbol{u}=0. \tag{1}$$

Using a cylindrical polar coordinate system, $(r,\theta,z)\in[0,1]\times[0,2\pi]\times[-0.5\Gamma,0.5\Gamma]$, with corresponding velocity $\boldsymbol{u}=(u,v,w)$ and vorticity $\nabla\times\boldsymbol{u}=(\chi,\eta,\zeta)$, the no-slip boundary conditions are:

$$\begin{aligned}
&r\in[0,1],\, z=-0.5\Gamma: && (u,v,w)=(0,r\mathrm{Re}\,[\epsilon-1],0),\\
&r\in[0,1],\, z=0.5\Gamma: && (u,v,w)=(0,r\mathrm{Re}\,[\epsilon+1],0),\\
&r=1,\, z\in[-0.5\Gamma,0): && (u,v,w)=(0,\ \mathrm{Re}\,[\epsilon-1],0),\\
&r=1,\, z\in(0,0.5\Gamma]: && (u,v,w)=(0,\ \mathrm{Re}\,[\epsilon+1],0).
\end{aligned} \tag{2}$$

The three governing parameters are

$$\begin{aligned}
&\text{Reynolds number:} && \mathrm{Re}=\omega a^2/\nu,\\
&\text{aspect ratio:} && \Gamma=h/a,\\
&\text{rotation defect:} && \epsilon.
\end{aligned} \tag{3}$$

The Navier–Stokes equations are solved with the same code as was used for $\epsilon=0$.[6] Briefly, it employs a second-order time-splitting method and space is discretized via a Galerkin–Fourier expansion in θ and Chebyshev collocation in r and z:

$$\boldsymbol{u}(r,\theta,z,t)=\sum_{i=0}^{2n_r+1}\sum_{j=0}^{n_z}\sum_{k=-n_\theta}^{n_\theta-1}\hat{\boldsymbol{u}}_{ijk}(t)\chi_i(r)\chi_j(\frac{2z}{\Gamma})\mathrm{e}^{\mathrm{i}k\theta}, \tag{4}$$

where χ_n is the nth Chebyshev polynomial. The modal kinetic energies, corresponding to azimuthal wavenumbers m, are

$$E_m=\frac{1}{2}\int_{-0.5\Gamma}^{0.5\Gamma}\int_0^1\boldsymbol{u}_m\cdot\boldsymbol{u}_m^*\,r\,\mathrm{d}r\,\mathrm{d}z, \tag{5}$$

where $\boldsymbol{u}_m$ is the mth Fourier component of the velocity field and $\boldsymbol{u}_m^*$ is its complex conjugate.

To avoid Gibb's phenomenon due to the discontinuity in the sidewall boundary condition for the azimuthal velocity, we regularized the boundary condition by smoothing the discontinuity over a small distance. Specifically, we replaced the boundary condition for the azimuthal velocity with

$$\begin{aligned}
&r=1,\, z\in[-0.5\Gamma,0): && v=\mathrm{Re}\,[1-\epsilon]\tanh(\delta z)\\
&r=1,\, z\in(0,0.5\Gamma]: && v=\mathrm{Re}\,[1+\epsilon]\tanh(\delta z),
\end{aligned} \tag{6}$$

where δ governs the distance over which the jump is smoothed; $\delta=50$ was used in this study, as was done in other related rotating split-cylinder studies.[6,22,23] Spatial resolution of $n_r=40$, $n_z=160$ and $n_\theta=32$, and time-step increments $\Delta t\in[10^{-4},10^{-5}]$ were used for the parameter range studied.

When the system is in exact counter rotation ($\epsilon=0$), it is invariant to two spatial symmetries: invariance to arbitrary rotations about the cylinder axis, $\mathcal{R}_\alpha$, and the

combined action of a reflection in the mid-plane $z = 0$ and a reflection in the meridional plane $\theta = 0$, $\mathcal{H}$. $\mathcal{R}_\alpha$ is isomorphic to the continous $SO(2)$ symmetry group and $\mathcal{H}$ is isomorphic to the discrete Z_2 symmetry group. The actions of $\mathcal{R}_\alpha$ and $\mathcal{H}$ on the velocity are

$$\begin{aligned} \mathcal{R}_\alpha &: [u,v,w](r,\theta,z,t) \mapsto [u,v,w](r,\theta+\alpha,z,t), \\ \mathcal{H} &: [u,v,w](r,\theta,z,t) \mapsto [u,-v,-w](r,-\theta,-z,t), \end{aligned} \tag{7}$$

where α is an arbitrary angle. Note that for solutions that are axisymmetric (i.e. $\mathcal{R}_\alpha$ invariant for any α), the action of $\mathcal{H}$ simply reduces to that of a reflection in the mid-plane, $\mathcal{K}$, whose action is

$$\mathcal{K} : [u,v,w](r,\theta,z,t) \mapsto [u,-v,-w](r,\theta,-z,t) \tag{8}$$

The two spatial symmetries, $\mathcal{R}_\alpha$ and $\mathcal{H}$, do not commute, and together they are isomorphic to the $O(2)$ symmetry group.[24] If $\epsilon \neq 0$, the system is no longer $\mathcal{H}$ invariant, but it continues to retain $\mathcal{R}_\alpha$ invariance.

For the present study, the aspect ratio was fixed to $\Gamma = 1.45$ and Re varied from 100 to 300. This choice of Γ was made as it is close to the 2:3 codimension-2 point in (Re, Γ) parameter space, where the $SO(2)$ symmetry is broken to states with either azimuthal wavenumbers $m = 2$ or $m = 3$ for the exact counter-rotating problem with $\epsilon = 0$ (see Fig. 2). The simulations were generally initiated with the $\epsilon = 0$ solution at the given Re and Γ, together with a random perturbation of order 10^{-15} in the $m = 1$ Fourier components, and continued to larger ϵ (typically using steps of 0.001 in ϵ). Additionally, an effort was made to identify possible hysteresis in the solutions. Therefore, for all the solution branches, the simulations were also restarted from a higher ϵ solution and continued to smaller ϵ.

III. OVERVIEW OF THE EXACTLY COUNTER-ROTATING CASE NEAR THE 2:3 INTERACTION

The exact counter-rotating case was studied in Gutierrez-Castillo and Lopez[6] for a variety of aspect ratios, $\Gamma \in [0.5, 2]$, and Reynolds numbers, $\mathrm{Re} \in [100, 300]$, showing very rich dynamics dominated by the strong shear layer in the center of the split cylinder. For the smallest values of Re, the basic state BS, which is steady and axisymmetry, is the unique solution. As Re is increased, BS loses stability breaking the azimuthal invariance, and typically a family of steady states, Sm, with different azimuthal wavenumbers m, are spawned. Some of these coexist, depending on the aspect ratio. When Re is further increased, the dynamics are dominated by m:$m+1$ interactions. Specifically, in the region with $\Gamma \sim 1.3$ and $\mathrm{Re} \sim 130$, the flow is dominated by the 2:3 interaction. Some of the main results in the neighborhood of this codimension-2 point are summarized here, as in the following section we shall consider the effects of small imperfections, $\epsilon \lesssim 0.01$, for nearby aspect ratio $\Gamma = 1.45$ and a range of Re.

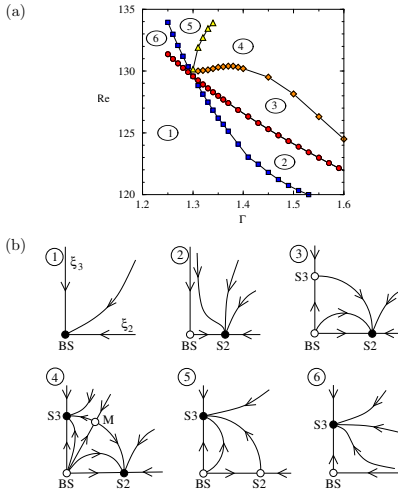

FIG. 2. (a) Bifurcations curves in (Γ, Re) parameter space in the neighborhood of a 2:3 interaction between S2 and S3. (b) Phase portraits in the 6 regions indicated in (a); ξ_2 and ξ_3 are phase space coordinates related to Γ and Re. The filled circles are stable states and the open circles are unstable states.

Figure 2(a) shows the bifurcation curves in (Γ, Re) parameter space with $\Gamma \in [1.2, 1.6]$ and Fig. 2(b) shows schematic phase portraits in the various regions of parameter space. In region ①, the only state is the steady axisymmetric basic state, BS. In the first bifurcation (with $\Gamma \gtrsim 1.3$), BS loses stability to a steady flow S2, with azimuthal wavenumber $m = 2$, which is stable and coexists with the now unstable BS in region ②. Crossing from region ② into region ③, the unstable BS undergoes another symmetry breaking bifurcation, spawning another steady state S3 with azimuthal wavenumber $m = 3$, which remains unstable in region ③. On crossing from region ③ into region ④, S3 undergoes a bifurcation in which it becomes stable as it spawns a mixed mode M. The mixed mode is a saddle state (unstable) with unstable manifolds connected to both S3 and S2, which are both stable in region ④. On traversing from region ④ to region ⑤, S2 undergoes a bifurcation, absorbing M and losing stability. Traversing from ⑤ to region ⑥, the unstable S2 is absorbed by BS, which remains unstable to S3. Finally, in traversing from region ⑥ back to region ①, the stable S3 is absorbed by BS at a bifurcation which renders BS stable. It is important to remark that this description is very local to the 2:3 interaction point, and that further afield in parameter space there is a multiplicity of stable solutions, including unsteady solutions, as described below.

Figure 3(a) shows how the primary non-axisymmetric modal energy for each of the bifurcating states varies

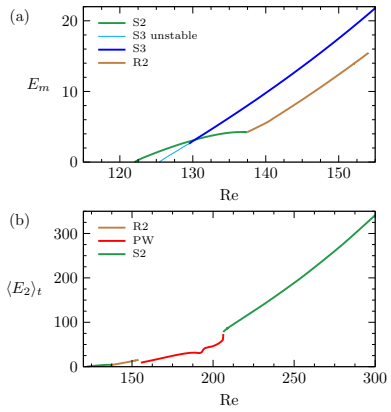

FIG. 3. (a) Variation with Re of the modal kinetic energies, E_m, with Re for the steady states S2 and S3 and the rotating wave R2, with $\Gamma = 1.45$ in exact counter rotation. The unstable S3 was computed in the $m = 3$ symmetric subspace. (b) Time-averaged modal kinetic energy $\langle E_2\rangle_t$ variation with Re, also with $\Gamma = 1.45$ in exact counter rotation, of S2, R2 and the pulse wave PW (E_2 is time invariant for S2 and R2).

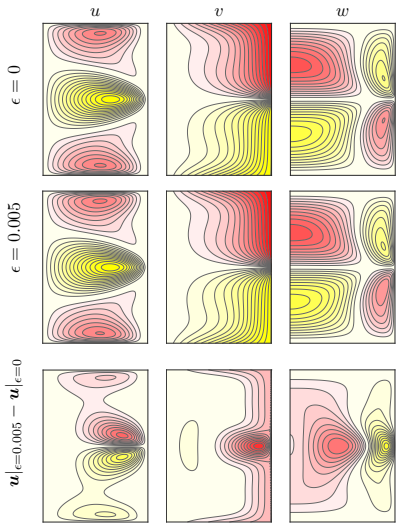

FIG. 4. Velocity contours in a (r, z)-meriodional plane of basic states at $\mathrm{Re} = 120$ and $\Gamma = 1.45$ for $\epsilon = 0$ (first row) and $\epsilon = 0.005$ (second row). The contour levels are $u, w \in [-0.18\mathrm{Re}, 0.18\mathrm{Re}]$, $v \in [-\mathrm{Re}, \mathrm{Re}]$. The third row the differences between the two; contours levels are $(u_\epsilon - u_0)$, $(w_\epsilon - w_0) \in [-0.75\epsilon\mathrm{Re}, 0.75\epsilon\mathrm{Re}]$ and $(v_\epsilon - v_0) \in [-3\epsilon\mathrm{Re}, 3\epsilon\mathrm{Re}]$; red is positive and yellow is negative.

with Re when $\Gamma = 1.45$ and $\epsilon = 0$. For $\mathrm{Re} \lesssim 137$, the situation is as described above with a traverse from region ①, through ② into region ③. At $\mathrm{Re} \approx 139$, S2 loses stability in a drift-Hopf bifurcation, spawning a rotating wave, R2, with $\mathcal{R}_\pi$ invariance; its rotation period is infinite at onset. The steady S3 continues to be stable in this parameter regime. Further increasing Re beyond approximately 155, R2 loses stability in a cyclic-fold bifurcation, giving rise to slow-fast dynamics in the form of a pulse wave, PW, which also has E_2 as the dominant non-axisymmetric modal kinetic energy, but unlike S2 and R2, this modal energy is not constant in time. Figure 3(b) shows how the time-averaged E_2 varies with Re for R2 and PW, as well as S2 at high Re. As $\mathrm{Re} \to 206$, PW undergoes a saddle-node-on-an-invariant-circle (SNIC) bifurcation and the flow collapses onto the steady S2.

In the following sections, we analyze the influence of the defect parameter ϵ on each solution type, focusing on their robustness.

IV. THE AXISYMMETRIC STEADY BASIC STATE

For Re and ϵ sufficiently small (the values are Γ-dependent), the flow is the steady axisymmetric basic state. The basic state for small ϵ is very similar to that at $\epsilon = 0$, except that the mid-plane reflection $\mathcal{K}$ is weakly broken. The dominant feature continues to be the shear layer about the mid-plane. Figure 4 shows contours of the three components of velocity of the basic states at $\mathrm{Re} = 120$ and $\Gamma = 1.45$ with $\epsilon = 0$ and 0.005. The flow with $\epsilon = 0$ is primarily in the azimuthal direction, but in opposite directions in each half of the cylinder; the flow would be solid-body rotation (i.e. vortex lines parallel to the cylinder axis) with $v = r\mathrm{Re}$ in the top half if not for the $-v$ flow in the bottom half. As such, the vortex lines are bent as they approach the mid-plane and all meet at the gap between the two counter-rotating cylinder halves, forming an azimuthal shear layer at the mid-plane whose axial thickness diminishes with increasing Re. This vortex line bending at the mid-plane drives a meridional flow. The radial component, u, is inwards away from the gap in the cylinder sidewall, and the axial component, w, is directed downwards along the top half-cylinder wall and upwards along the bottom half-cylinder wall, meeting at the mid-plane. This meridional flow is closed by weaker radial outflows along the top and bottom endwalls and axial flows away from the mid-plane into the interior. The strength of the meridional flow is approximately 20% of the strength of the azimuthal flow. With $\epsilon = 0.005$, the flow is little changed, and the differences are very subtle to spot by simply comparing the velocity component contour plots. The third row of Fig. 4 shows the differences between the $\epsilon = 0.005$ and $\epsilon = 0$ basic states. Having added $\epsilon\mathrm{Re}$ to the rotation rates of both cylinder halves, we see that the difference in v is positive almost

everywhere, with a maximum on the midplane close to the sidewall. What is perhaps unexpected is that the maximum value in this difference is large, approximately $3\epsilon\mathrm{Re}$. The maximal differences in the meridional components are commensurately smaller, of order $\pm 0.75\epsilon\mathrm{Re}$, with the axial flow difference being greatest in the sidewall layer at the mid-plane and directed downwards, and the radial flow differences are greatest above and below the mid-plane at the edge of the sidewall layer, with the radial flow difference being outwards above and inwards below the mid-plane.

V. SPONTANEOUS BREAKING OF AXISYMMETRY

When $\epsilon = 0$, as Re is increased the basic state undergoes a bifurcation breaking axisymmetry, and non-axisymmetric steady solutions exist with different azimuthal wavenumbers, depending on Γ. In the region around $\Gamma = 1.45$, steady states with azimuthal wavenumbers $m = 2$ and 3 (S2 and S3) coexist in range a of Re, as shown in Fig. 2(a). This (Γ, Re) parameter regime is interesting to explore the impact of $\epsilon \neq 0$ due to the multiplicity of stable solutions for $\epsilon = 0$. The next subsections analyze the influence of ϵ on the various non-axisymmetric exactly counter-rotating states described in §III. Specifically, for $\Gamma = 1.45$, we consider the consequences of increasing ϵ on S3 and S2 at $\mathrm{Re} = 135$, where for $\epsilon = 0$ these are in region ④ of Fig. 2 and are both stable, PW at $\mathrm{Re} = 160$ and S2 at $\mathrm{Re} = 300$ which are both removed from the 2:3 codimension-2 point.

A. Solutions for $\mathrm{Re} = 135$ starting from S3

With the introduction of imperfection, $\epsilon \ll 1$, the S3 steady state at $\mathrm{Re} = 135$ and $\Gamma = 1.45$ (in region ④ of Fig. 2) at $\epsilon = 0$ becomes a very slowly rotating wave, R3, retaining the $m = 3$ symmetry, i.e. invariance to $\mathcal{R}_{2\pi/3}$. The spatial structure of R3 is very similar to S3, with the same level of weakly broken mid-plane reflection effects as described earlier for the basic state; but instead of the structure being stationary, it is rotating with a very slow frequency. In general, R_m are rotating waves with azimuthal wavenumber m: $\boldsymbol{u}(r,\theta,z,t) = \boldsymbol{u}(r,\theta + 2\pi/m, z, t)$. The rotation period, τ_R, is the time for the wave to rotate though 2π. For rotating waves, a rotation about the axis is equivalent to a time translation: $\boldsymbol{u}(r,\theta-\alpha,z,t) = \boldsymbol{u}(r,\theta,z,t+\alpha\tau_R/2\pi)$.

With increasing ϵ, the solutions remain rotating waves, but their periods diminish from very large values at small ϵ. Figure 5 shows how the rotation period of R3, $\tau_R \to \infty$ as $\epsilon \to 0$. This makes for very long simulation times to confirm that the solution is indeed a rotating wave, as several periods need to be computed. We were able to compute down to $\epsilon = 0.0001$, confirming that the solution is R3 rather than S3 for small $\epsilon \neq 0$. Figure 6 and the corresponding integral multimedia `movie-1.avi` show isosurfaces of the axial velocity for an example of R3 at $\mathrm{Re} = 135$, $\Gamma = 1.45$ and $\epsilon = 0.007$ over the rotation period τ_R, illustrating that the flow structure remains invariant and rotates uniformally about the axis.

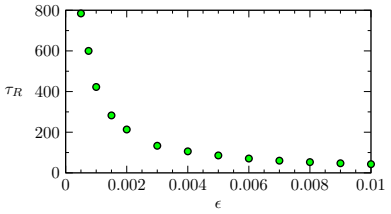

FIG. 5. Variation with ϵ of the rotation period τ_R of R_3, at $\mathrm{Re} = 135$ and $\Gamma = 1.45$.

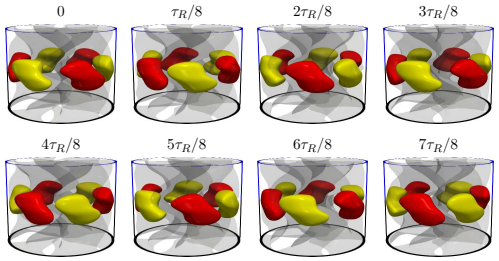

FIG. 6. Isosurfaces of the axial velocity, w, of R3 at $\mathrm{Re} = 135$, $\Gamma = 1.45$ and $\epsilon = 0.007$ over one rotation period τ_R. See the integral multimedia `movie-1.avi` for an animation over $\tau_R = 60.0$.

B. Solutions for $\mathrm{Re} = 135$ starting from S2

We now consider the effects of $\epsilon \neq 0$ on S2 at the same $\mathrm{Re} = 135$ and $\Gamma = 1.45$ as was considered for S3 in the previous subsection. This is a parameter point in region ④ where S2 and S3 are both stable when $\epsilon = 0$. Unlike the S3 response, the introduction of $\epsilon \neq 0$ results in the steady S2 transforming into a pulse wave with slow-fast dynamics, rather than a rotating wave. As was illustrated in Fig. 3(b), pulse waves PW were found for $\epsilon = 0$ at $\Gamma = 1.45$, but at significantly larger $\mathrm{Re} \gtrsim 155$, where they originate in a drift-Hopf bifurcation from a rotating wave R2.[6] The pulse waves found for $\epsilon \neq 0$ are different from PW; they are pulse waves with an additional background rotation. Hence, we call them rotating pulse waves RPW.

These RPW are quasiperiodic; one period corresponds to the background rotation which is analogous to the period of a rotating wave, τ_R, and the other to the pulse, τ_P. The time series shown in Fig. 7 are of the radial velocity at a point, $u_p = u(r = 0.98, \theta = 0, z = 0)$, and of the modal kinetic energy E_2 of the rotating pulse

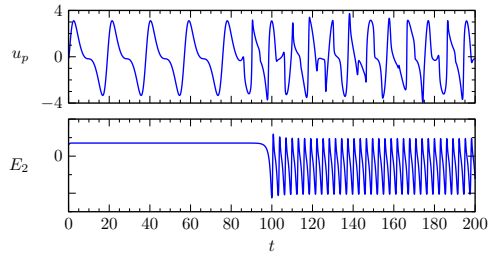

FIG. 7. Time evolution of $u_p = u(r = 0.98, \theta = 0, z = 0)$ and the modal kinetic energy E_2 of the rotating pulse wave RPW at $(\Gamma, \mathrm{Re}) = (1.45, 135)$ for $\epsilon = 0.003$.

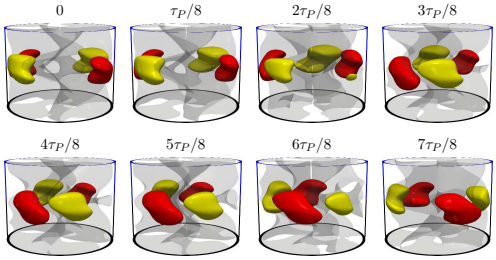

FIG. 8. Isosurface of w over one pulse period $\tau_P = 4.08$ of RPW at $\mathrm{Re} = 135$, $\Gamma = 1.45$ and $\epsilon = 0.003$. The integral multimedia movie-2.avi shows an animation over a rotating period $\tau_R = 20$.

wave RPW at $\mathrm{Re} = 135$, $\Gamma = 1.45$ and $\epsilon = 0.003$. The initial transient is essentially a rotating wave with $m = 2$: E_2 is constant while u_p oscillates with period $\tau_R/2$ (the factor of 2 coming from the $m = 2$ spatial symmetry). By time $t \approx 100$, there is a change in the character of the time series; E_2 now has a regular periodicity, with a period we call τ_p, whereas u_p is quasiperiodic. Figure 8 shows snapshots of RPW at $\mathrm{Re} = 135$, $\Gamma = 1.45$ and $\epsilon = 0.003$ over a pulse period τ_P. To further appreciate that RPW flow has a uniform background rotation in addition to the slow-fast pulse dynamics, the integral multimedia movie-2.avi shows an animation over a rotating period $\tau_R = 20 \approx 4.9\tau_p$, from which it is easier to see the pulse, a quick change in the structure of the solution, whilst the whole structure rotates almost uniformly.

To further appreciate the cause of the pulses, Fig. 9 shows time series (after transients have died off, and arbitrarily resetting $t = 0$ at the start of the displayed series) of the modal kinetic energies, E_2 and E_3, for various ϵ whilst keeping $\mathrm{Re} = 135$, $\Gamma = 1.45$, and using S2 at $\epsilon = 0$ as the initial condition. At $\epsilon = 0$, S2 has $E_3 = 0$ and E_2 is steady. For small ϵ, E_2 remains steady (at a level essentially corresponding to that at $\epsilon = 0$), except for very short bursts that occur periodically (corresponding to τ_P). For the times in between the pulses, the steady

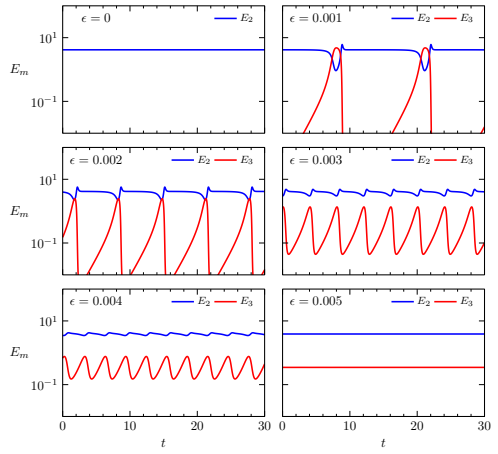

FIG. 9. Time series of the modal kinetic energies E_2 and E_3 for $\mathrm{Re} = 135$ and $\Gamma = 1.45$, starting from S2 (for convenience, the initial time is shown as $t = 0$ for each case; the time series are presented after allowing for transients to die off) and ϵ as indicated. E_m for $m > 0$ that are not shown are orders of magnitude smaller than those shown.

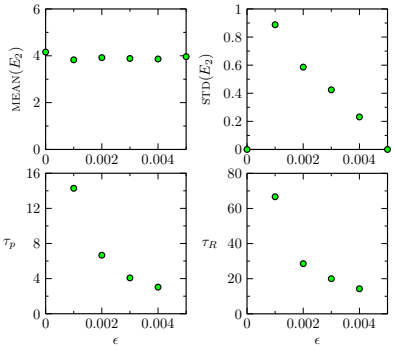

FIG. 10. Variations with ϵ of the mean and standard deviation of E_2, together with τ_p and τ_R, for rotating pulse waves RPW at $\mathrm{Re} = 135$ and $\Gamma = 1.45$, determined from the time series in Fig. 9.

E_2 corresponds to a rotation (see integral multimedia movie-2.avi). The pulses correspond to the exponential growth in E_3 from very small levels (essentially machine zero for the smallest non-zero ϵ), and when it grows to be comparable to E_2, there is a rapid nonlinear interaction between the azimuthal components of the flow followed by a near instantaneous collapse in E_3 leaving the slow rotating wave with $m = 2$. With increasing ϵ, the pulse interaction between azimuthal modes occurs while E_3 is processively smaller than E_2, and the collapse in

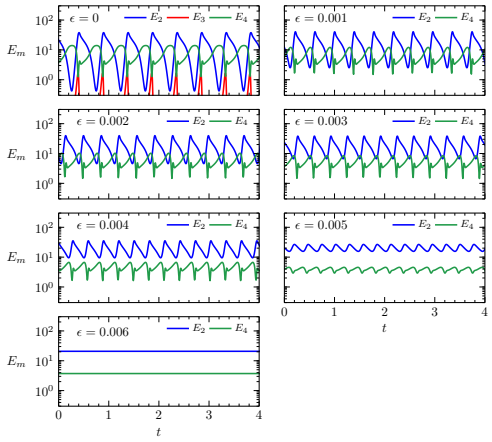

FIG. 11. Time series of the modal kinetic energies E_2, E_3 and E_4 for Re = 160 and $\Gamma = 1.45$, starting from PW (initial time has been reset to $t = 0$ for each case) and ϵ as indicated. E_m for $m > 0$ that are not shown are orders of magnitude smaller than those shown.

E_3 is less severe. As $\epsilon \to 0.005$, the amplitudes in the oscillations of E_2 and E_3 (quantified by their standard deviations) diminish, and for $\epsilon \gtrsim 0.005$, they are steady. The flow is a rotating wave, R1, with rotation period τ_R, and since it has non-zero E_2 and E_3, it only has invariance to $\mathcal{R}_{2\pi}$. Figure 10 summarizes the main features of RPW, showing how the mean and standard deviation of E_2, together with τ_p and τ_R, for RPW at Re = 135 and $\Gamma = 1.45$ vary with ϵ.

In this parameter regime, where both S2 and S3 are stable for $\epsilon = 0$, we have taken the RPW at $\epsilon = 0.005$, which has E_2 dominating over E_3, as the initial condition for a simulation with $\epsilon = 0$ and found that the flow evolves to S3, rather than S2. This further illustrates the richness in the dynamics in the neighborhood of the 2:3 interaction.

C. Solutions for Re = 160 starting from PW

For $\epsilon = 0$, at Re = 160 and $\Gamma = 1.45$, one of the stable states is a pulse wave PW, as described in Gutierrez-Castillo and Lopez [6] (see Fig. 3b). This pulse wave, like RPW described in the previous subsection, has E_3 periodically growing exponentially leading to a nonlinear interaction between azimuthal components of the flow, followed by a rapid decay in E_3. However, it differs from RPW in that during the long intervals when E_3 is very small, E_2 is not (essentially) constant, and E_4 is also active (in the sense that the $m = 4$ azimuthal component of the flow is not simply the second harmonic of the $m = 2$ azimuthal component, which it is for RPW). The first

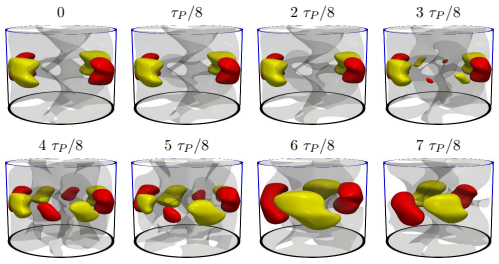

FIG. 12. Snapshots of w isosurfaces for PW at Re = 160, $\Gamma = 1.45$ and $\epsilon = 0.001$ over one pulse period $\tau_P = 0.39$. See integral multimedia movie-3.avi for an animation over $4\tau_P$.

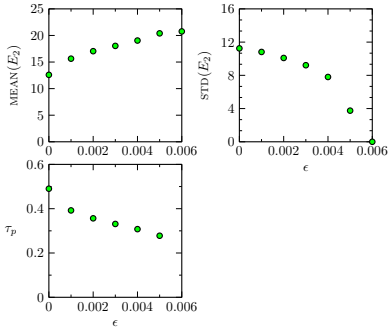

FIG. 13. The mean, standard deviation and period of the modal kinetic energy E_2 of PW at Re = 160 and $\Gamma = 1.45$ as a function of ϵ, determined from the time series in Fig. 11.

panel of Fig. 11, corresponding to $\epsilon = 0$, shows times series of E_2, E_3 and E_4, illustrating this complicated azimuthal interaction.

Introducing $\epsilon \neq 0$ and using the $\epsilon = 0$ PW as an initial condition results in a pulse wave in which E_3 has collapsed to machine noise. This is a case of introducing a symmetry-breaking imperfection ($\epsilon \neq 0$ breaks $\mathcal{H}$) results in added symmetry (from $\mathcal{R}_{2\pi}$ for $\epsilon = 0$ to $\mathcal{R}_\pi$ for $\epsilon \neq 0$). The flow is still a pulse wave, but now it is due to a periodic interaction between the $m = 2$ and $m = 4$ azimuthal components. Since the $m = 4$ flow component also includes a contribution from the second harmonic of the $m = 2$ component, this interaction is more complicated than the 2:3 interaction in RPW (since the $m = 2$ and $m = 3$ flow components are orthogonal). The time series in Fig. 11 show how for sufficiently small ϵ, there are time intervals during which $E_4 > E_2$. Figure 12 shows snapshots of w for PW over a pulse period τ_p at $\epsilon = 0.001$, from which it is evident that most snap-shots have $\mathcal{R}_\pi$ symmetry, but at about phase $3\tau_P/8$ there is a spatial period-doubling. All of this is better appreciated in the integral multimedia movie-3.avi which animates these isosurfaces over $4\tau_p$. These representations illustrate how

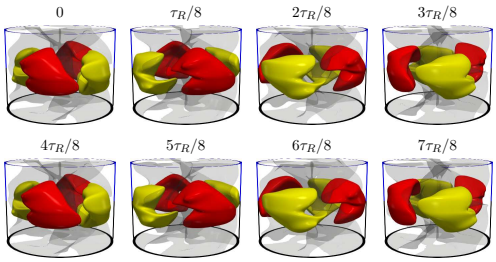

FIG. 14. Snapshots of w isosurfaces for R2 at Re $= 300$ and $\Gamma = 1.45$, and $\epsilon = 0.007$ over one rotation period τ_R. See integral multimedia movie-4.avi for an animation over $\tau_R = 8.33$.

the flow consists of two pairs of blobs of w that are related by the $\mathcal{R}_\pi$ symmetry, but during other intervals (when $E_4 > E_2$), there are four pairs related by $\mathcal{R}_{\pi/2}$. With increasing ϵ, E_4 remains substantially below E_2, and as $\epsilon \to 0.006$, the $m = 4$ flow component simply becomes the second harmonic of the $m = 2$ component, and the flow is a rotating wave R2 with $\mathcal{R}_\pi$ invariance (and hence all modal energies are constant in time). Figure 13 summarizes the main features of PW, showing how the mean and standard deviation of E2, together with τ_p. In contrast with RPW, the mean E_2 grows with ϵ, and τ_p is very much smaller and has less variation with ϵ. This is very likely due to the fact that here the $\epsilon = 0$ is already a pulse wave, whereas for the RPW described in the previous subsection, the $\epsilon = 0$ state was steady, and the introduction of $\epsilon \neq 0$ was akin to a depinning with a resultant infinite period forced symmetry breaking bifurcation.

D. Solutions for Re $= 300$ starting from S2

We now consider the effects of $\epsilon \neq 0$ far from the 2:3 interaction, at Re $= 300$ and $\Gamma = 1.45$ where S2 is stable there is no interaction between modes 2 and 3 for $\epsilon = 0$ (see Fig. 3b). Using S2 as the initial condition for simulations with $\epsilon \neq 0$ results in a rotating wave R2 with $\mathcal{R}_\pi$ invariance; there is no sign of mode 3 contribution. Figure 14 shows snapshots of w over a rotation period $\tau_R = 8.33$ for R2 at $\epsilon = 0.007$. The integral multimedia movie-4.avi animates this over τ_R, clearly showing the flow to be a rotating wave. Figure 15 shows how τ_R varies with ϵ; again $\tau_R \to \infty$ as $\epsilon \to 0$, indicative of the defect leading to a depinning from the steady S2 at $\epsilon = 0$ to the slowing rotating R2 for $\epsilon \gtrsim 0$.

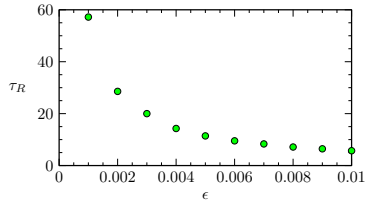

FIG. 15. Period of a full rotation of the R2 for Re $= 300$ with respect to the defect parameter ϵ.

VI. DISCUSSION AND CONCLUSIONS

We have considered the effects of an imperfection on the dynamics of the flow in a cylinder split in half at the axial midplane and the two halves counter-rotating. In the absence of the imperfection, the two halves are in exact counter rotation, and the system has $O(2)$ symmetry. The continuous part of the $O(2)$ group, $SO(2)$, corresponds to invariance around the axis, i.e. the system is axisymmetric, and the discrete Z_2 part corresponds to a reflection about the midplane $z = 0$ together with a reflection about the meridional plane $\theta = 0$. Forcing a small difference in the rotation rates of the two halves, quantified by a small parameter ϵ, weakly breaks the Z_2 symmetry, but leaves the $SO(2)$ symmetry intact. How the axisymmetry breaks spontaneously when $\epsilon \neq 0$ differs from the $\epsilon = 0$ scenarios. We focus our attention on parameter regimes close to a codimension-2 point in Reynold number–aspect ratio parameter space where for $\epsilon = 0$ there is a complex interaction between two steady states that have both spontaneously broken $SO(2)$ symmetry, one having azimuthal wavenumber $m = 2$ and the other $m = 3$. Particularly interesting dynamical states in the neighborhood of this 2:3 interaction are pulse waves, in which the steady non-axisymmetric structures suddenly change their azimuthal positions in a periodic, but slow-fast fashion. In other related problems with $O(2)$ symmetry, the 1:2 interaction has been extensively studied. In those systems, the interesting dynamics are associated with heteroclinic cycles. In studying the effects of breaking the Z_2 component of $O(2)$ whilst retaining the $SO(2)$ component, Chossat [11] showed that this forced symmetry breaking destroys the heteroclinic cycles.

In forcing the breaking of Z_2 and retaining $SO(2)$ in the neighborhood of the 2:3 interaction, we find that the pulse waves persist, and in some parameter regimes a pulse wave with an additional slow background rotation (due to the spontaneously broken $SO(2)$ symmetry) were also found. At sufficiently large $\epsilon \sim 0.006$, the pulse waves collapse to rotating waves, with much simpler dynamics. It is not too surprising that with increasing ϵ the dynamic simplifies to that of a rotating wave. As ϵ is increased, the system is driven further away from an $O(2)$ invariant system, where steady non-axisymmetric states are generically the first to spontaneously bifurcate, to-

wards an $SO(2)$ invariant system. For $SO(2)$ invariant systems, the generic results of symmetry breaking bifurcations are rotating waves.

ACKNOWLEDGMENTS

We thank ASU Research Computing facilities. This work was supported in part by the U.S. National Science Foundation grant 1929139.

DATA AVAILABILITY

The data that support the findings of this study are available from the corresponding author upon reasonable request.

[1]G. Luo and T. Y. Hou, "Potentially singular solutions of the 3D axisymmetric Euler equations," Proc. Nat. Acad. Sci. USA **111**, 12968–12973 (2014).
[2]D. Chae and T.-P. Tsai, "Remark on Luo–Hou's ansatz for a self-similar solution to the 3D Euler equations," J. Nonlinear Sci. **25**, 193–202 (2015).
[3]G. Sperone, "Further remarks on the Luo–Hou's ansatz for a self-similar solution to the 3D Euler equations," J. Nonlinear Sci. **27**, 1325–1338 (2017).
[4]G. Luo and T. Y. Hou, "Formation of finite-time singularities in the 3D axisymmetric Euler equations: A numerics guided study," SIAM Review **61**, 793–835 (2019).
[5]D. Barkley, "A fluid mechanic's analysis of the teacup singularity," Proc. Roy. Soc. Lond. A **476**, 20200348 (2020).
[6]P. Gutierrez-Castillo and J. M. Lopez, "Nonlinear mode interactions in a counter-rotating split-cylinder flow," J. Fluid Mech. **816**, 719–745 (2017).
[7]C. Nore, L. S. Tuckerman, O. Daube, and S. Xin, "The 1:2 mode interaction in exactly counter-rotating von Kármán swirling flow," J. Fluid Mech. **477**, 51–88 (2003).
[8]J. D. Crawford and E. Knobloch, "Classification and unfolding of degenerate Hopf bifurcations with O(2) symmetry: no distinguished parameter," Physica D **31**, 1–148 (1988).
[9]J. D. Crawford and E. Knobloch, "On degenerate Hopf bifurcation with broken O(2) symmetry," Nonlinearity **1**, 617–652 (1988).
[10]E. Knobloch, "Symmetry and instability in rotating hydrodynamic and magnetohydrodynamic flows," Phys. Fluids **8**, 1446–1454 (1996).
[11]P. Chossat, "Forced reflectional symmetry breaking of an O(2)-symmetric homoclinic cycle," Nonlinearity **6**, 723–731 (1993).
[12]J. O. Rodriguez-Garcia and J. Burguete, "Experimental lateral wall boundary layer behavior of a differentially rotating split-cylinder flow," Phys. Rev. E **99**, 023111 (2019).
[13]J. R. Pacheco, J. M. Lopez, and F. Marques, "Pinning of rotating waves to defects in finite Taylor–Couette flow," J. Fluid Mech. **666**, 254–272 (2011).
[14]F. Marques, A. Meseguer, J. M. Lopez, J. R. Pacheco, and J. M. Lopez, "Bifurcations with imperfect SO(2) symmetry and pinning of rotating waves," Proc. Roy. Soc. Lond. A **469**, 20120348 (2013).
[15]J. Abshagen, M. Heise, C. Hoffmann, and G. Pfister, "Direction reversal of a rotating wave in Taylor-Couette flow," J. Fluid Mech. **607**, 199–208 (2008).
[16]B. Garbin, J. Fatome, G. L. Oppo, M. Erkintalo, S. Murdoch, and S. Coen, "Asymmetric balance in symmetry breaking," Phys. Rev. Research **2**, 023244 (2020).
[17]A. de la Torre and J. Burguete, "Slow dynamics in a turbulent von Kármán swirling flow," Phys. Rev. Lett. **99**, 054101 (2007).
[18]E. Crespo del Arco, J. J. Sánchez-Álvarez, E. Serre, A. de la Torre, and J. Burguete, "Numerical and experimental study of the time-dependent states and the slow dynamics in a von Kármán swirling flow," Geophys. Astrophys. Fluid Dyn. **103**, 163–177 (2009).
[19]P. P. Cortet, A. Chiffaudel, F. Daviaud, and B. Dubrulle, "Experimental evidence of a phase transition in a closed turbulent flow," Phys. Rev. Lett. **105**, 214501 (2010).
[20]C. Nore, F. Moisy, and L. Quartier, "Experimental observation of near-heteroclinic cycles in the von Kármán swirling flow," Phys. Fluids **17**, 064103 (2005).
[21]J. Porter and E. Knobloch, "Dynamics in the 1:2 spatial resonance with broken reflection symmetry," Physica D **201**, 318–344 (2005).
[22]P. Gutierrez-Castillo and J. M. Lopez, "Instabilities of the sidewall boundary layer in a rapidly rotating split cylinder," Eur. J. Mech. B-Fluids **52**, 76–84 (2015).
[23]J. M. Lopez and P. Gutierrez-Castillo, "Three-dimensional instabilities and inertial waves in a rapidly rotating split-cylinder flow," J. Fluid Mech. **800**, 666–687 (2016).
[24]C. Nore, L. M. Witkowski, E. Foucault, J. Pécheux, O. Daube, and P. Le Quéré, "Competition between axisymmetric and three-dimensional patterns between exactly counter-rotating disks," Phys. Fluids **18**, 054102 (2006).